Measurement 205 (2022) 112182

Contents lists available at ScienceDirect

Measurement

journal homepage: www.elsevier.com/locate/measurement

Misalignment angle calibration of semi-active laser seeker based on locally weighted scatterplot smoothing and interpolation method

Mingyue Zhang [a,*], Hui Liu [b], Yongliang Guan [c], Qingdang Li [a], Zhen Sun [a]

[a] College of Sino-German Science and Technology, Qingdao University of Science and Technology, Qingdao 266061, China
[b] Changchun Institute of Optics, Fine Mechanics and Physics, Chinese Academy of Sciences, No. 3888, Dongnanhu Rd., Changchun 130033, Jilin, China
[c] Chang Guang Satellite Technology Co., LTD, Changchun 130033, China

ARTICLE INFO

Keywords:
Five-axis turntable
Misalignment angle calibration
Semi-active laser seeker
Lowess

ABSTRACT

The accuracy of the misalignment angle affects the precision of missile systems. Owing to systematic errors and random errors, the misalignment angle measured by the seeker detector deviates from the ideal misalignment angle. To improve the accuracy of the misalignment angle, this paper proposes the locally weighted scatterplot smoothing (Lowess) and the interpolation method to calibrate the misalignment angle. First, the model and error analysis of the misalignment angle are presented in the paper. Second, the proposed calibration strategy based on Lowess and the interpolation method is presented. Finally, calibration experiments are carried out to verify the excellent performance of the proposed calibration strategy. The experimental results show that the proposed calibrated strategy outperforms the currently used techniques and increases the misalignment angle precision.

1. Introduction

The seeker is an essential part of modern precision guidance systems. It is mostly used for tracking, measurement, and autonomous target search. The lethality of laser-guided weapons directly depends on the seeker's performance [1]. The advantages of semi-active laser guidance technology include higher guidance accuracy and potent anti-jamming capabilities. The fundamental principle of semi-active laser guidance is as follows. The carrier's (like an aircraft or ship's) laser designator is used to emit an encoded laser signal and illuminate the target. The laser signal that the target reflects is continuously picked up by the missile's seeker. The misalignment angle (pitch angle and yaw angle) between the target and the seeker's optical axis is then calculated [2]. As a result, the seeker may follow the target in real time based on its location. The guidance system then adjusts the missile's course based on the seeker data until it precisely hits the target. The correctness of the misalignment angle affects target location performance. If the misalignment angle is accurate, the missile can pinpoint the target with tremendous precision. A high level of accuracy in the misalignment angle is consequently required for the missile system to locate the target accurately [3,4].

The seeker system determines the misalignment angle [5]. It often deviates from the ideal misalignment angle for a variety of reasons, including mechanical processing, assembly, device accuracy, and others. To increase misalignment angle accuracy, there are typically two basic approaches used. The first method is to improve the system components and the processing technology. (1) The misalignment angle accuracy can be effectively improved by optimizing the structural design and improving the processing technology. (2) The misalignment angle accuracy can be effectively improved by adopting high-precision system components. However, excessively increasing the system composition accuracy will result in a large rise in the production cycle and cost of the opto-mechanical system. The accuracy of inertial guidance systems can be increased through calibration, as is widely known. As the centerpiece of an missile system, the seeker must also be calibrated. As a result, system calibration is the second method that is always used to improve misalignment angle accuracy [4,6]. The accuracy of the misalignment angle directly affects the positioning accuracy of the missile system [7]. It is possible to guarantee that the missile will hit its target precisely if the misalignment angles are calibrated. Attack mission will not be accomplished if misalignment angle precision is poor. System performance may be enhanced by the effective calibration process design.

Calibration model computation and calibration compensation work together to produce an accurate misalignment angle. There are two techniques for calculating calibration models: basic calibration techniques and advanced calibration techniques. Regression with

* Corresponding author.
E-mail address: zyy_2011@163.com (M. Zhang).

https://doi.org/10.1016/j.measurement.2022.112182
Received 14 July 2022; Received in revised form 29 October 2022; Accepted 5 November 2022
Available online 13 November 2022
0263-2241/© 2022 Elsevier Ltd. All rights reserved.

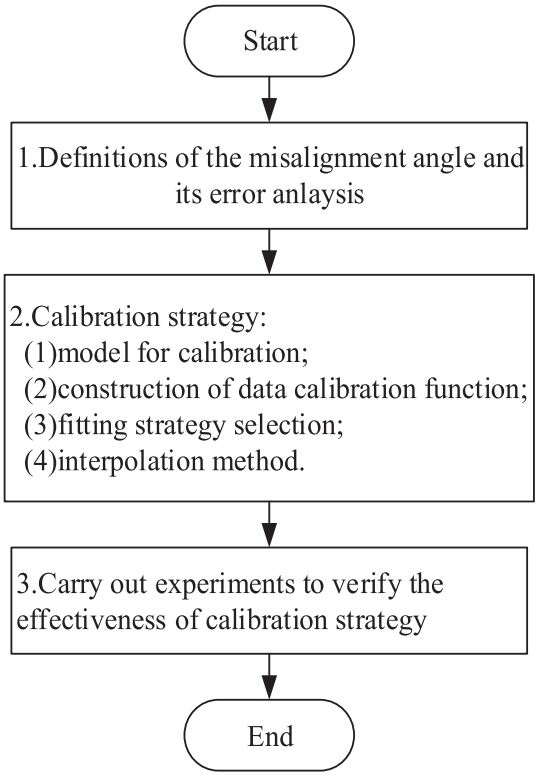

Fig. 1. Research flow chart of the paper.

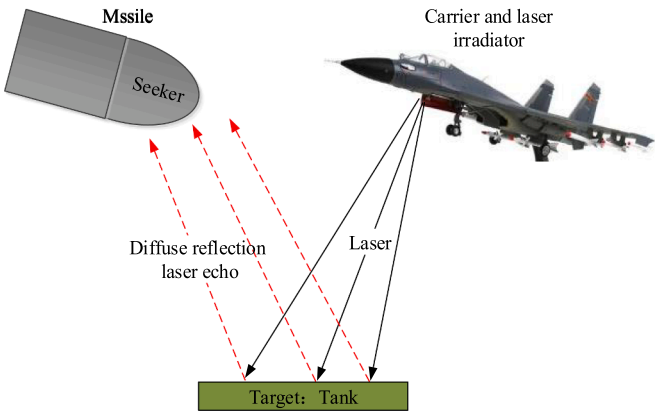

Fig. 2. Tracking schematic of the semi-active laser seeker.

parameter-based linearization [6,8] and polynomial fitting[9] are used as the basic calibration technique. The following concepts govern how the parameter-based linearization regression operates. To start, all the data are trained to produce a set of parameters for the training model. Second, the new sample is predicted using the training parameters. Because the prediction data only depend on the trained parameters, the original training data have no bearing on them. It is clear that the model parameters are established regardless of how many predictions of data are made in the future. Over a small range of angles, this technique is effective for misalignment angle calibration, but it fails over a greater range of angles [10]. A common technique for parameter modeling is polynomial fitting. It benefits from simple implementation and the absence of sophisticated data requirements. However, high-order systems are prone to instability, and the fitting curve deviates from the numerical range [9]. In addition, many scholars have also studied advanced calibration methods. The genetic algorithm is used to simultaneously calibrate the internal and external Doppler velocity log errors [11]. Particle swarm optimization is proposed to calibrate the Doppler velocity log[12]. A robust H ∞ estimation scheme is designed for in-flight calibration of UAVs with low-cost IMU[13]. Although the calibration is realized by these researchers, the advanced algorithm design has many parameters. The algorithm's debugging and optimization processes are also complicated. Based on the analysis above, this study presents novel methods for calibration by upgrading traditional methods. Adopting an algorithm with good robustness and powerful global search capabilities is crucial [14].

The non-parametric regression strategy is different from the fitting method described above. The prior data will be retrained to acquire new parameter values if a fresh sample is projected [15]. Therefore, the parameter values that are determined each time are uncertain. This principle's fitting technique is called locally weighted regression. The key idea behind the locally weighted scatterplot smoothing (Lowess) approach is to use a particular percentage of local data to fit a polynomial regression curve [16]. So, it is possible to see the local data's law and trend [17]. It can be used in numerous system fittings [18,19]. The misalignment angle is influenced by a wide range of variables, and its value exhibits nonlinear properties. Consequently, the misalignment angle may be calibrated very effectively using this non-parametric regression method.

As mentioned earlier, the calibration model calculation and calibration compensation work together to produce the precise misalignment angle. In this study, the calibration calculation model is developed using Lowess and calibration trials. In accordance with the calibrated model, calibration compensation is utilized to forecast the calibration data [20]. The interpolation method can be used for calibration compensation. The interpolation method is an approximate calculation method that can be used to approximate unknown points from known points [21,22]. The interpolation method includes linear interpolation [23], spline interpolation [24], nearest neighbor interpolation, spatial interpolation [25], and so on [26,27]. This paper use the linear interpolation technique to forecast the values in the calibration model due to its ease of use and simplicity [28,29].

Based on the research presented above, this paper suggests a Lowess and interpolation-based calibration procedure for the semi-active laser seeker's misalignment angle. The following are the primary contributions of this work in comparison to earlier research:

A new calibration strategy consisting of Lowess and an interpolation method is proposed. It includes model design, analysis, and performance verification.
The new calibration method is demonstrated by applying it to a specific seeker. The seeker and other systems can both be used with this technique.
For calibration, a traversal measuring method is developed. Two-dimensional data are acquired using this measurement method for real calibration.

The difference from other previously published works on the present subject is that here the non-parametric regression method and interpolation method are used here to improve the misalignment angle accuracy.

This paper proposes a method for calibrating the misalignment angle of the seeker. The research involves the definition and measurement principle of the misalignment angle of the seeker. The experimental apparatus consists of QD, a five-axis turntable, and other measuring equipment. The interpolation method processes the measurement data, and its ultimate purpose is to improve the measurement accuracy. Each part of the research content of this paper satisfies the scope of this journal.

This paper is organized as follows. In Section 2, the principle of a semi-active laser seeker is introduced, and the factors affecting misalignment angle accuracy are analyzed. The procedure for calibrating the misalignment angle is provided in Section 3. Section 4 provides

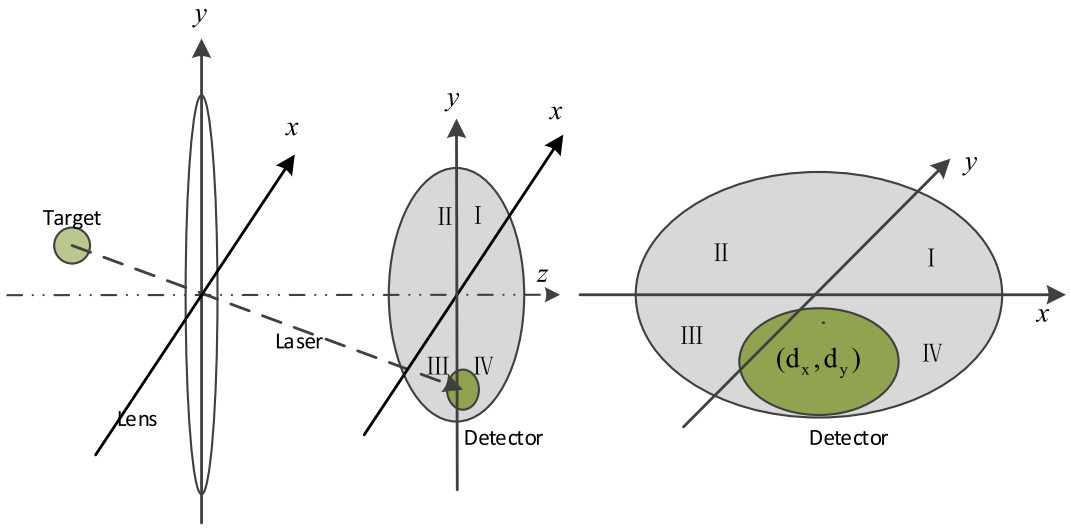

Fig. 3. Misalignment angle detection principle of the four quadrant APD.

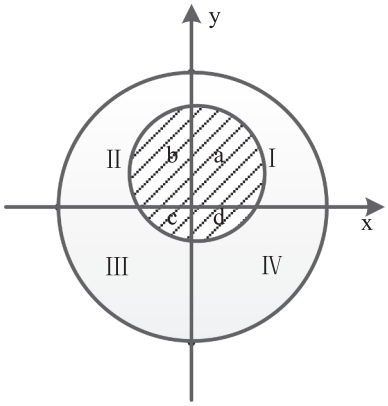

Fig. 4. Schematic diagram of the working principle of the four-quadrant detector.

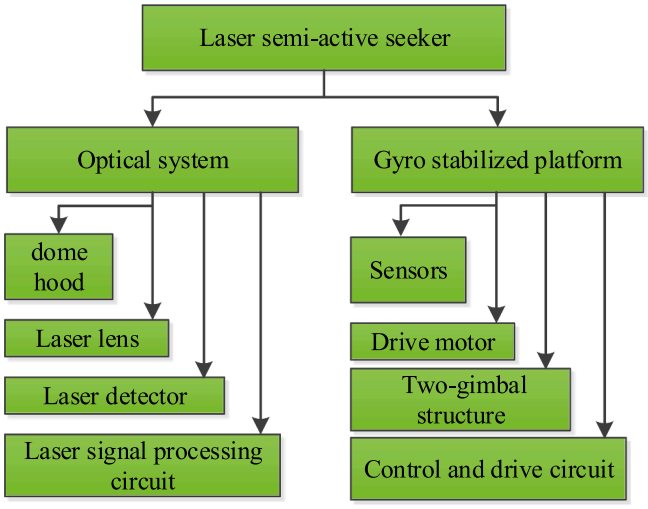

Fig. 5. Structure composition diagram of a semi-active laser seeker.

the experiments to verify the effectiveness of the calibration method. The results of the experiments demonstrate that the suggested calibration approach significantly increases the accuracy of the misalignment angle.

2. Problem statement

The research flow chart of this paper is shown in Fig. 1. The whole research consists of three parts. The misalignment angle's definition and error analysis are covered in the first section. The calibration strategy research is the second component. The development and verification of experiments makes up the third component. The descriptions of these three components can be found in Sections 2, 3, and 4, respectively.

2.1. Misalignment angle definitions and resolution methods

The tracking strategy for the semi-active laser seeker is shown in Fig. 2. The target diffusely reflects the laser signal that is from the airplane's laser emitting unit. The missile's laser seeker measures the target's reflection to determine the misalignment angle. The seeker's stabilized platform is moved according to the misalignment angle. The stabilized platform of the seeker is used to reduce the misalignment angle and ensure that the target is situated at the center of the optical axis of the seeker. The low accuracy of the misalignment angle affects the system's guidance.

In order to calculate the misalignment angle, the laser tracking system often employs a four-quadrant avalanche photo diode (APD), which frequently has a circular design (shown in Fig. 3). The quadrant detector (QD) is a device consisting of four separate photodetectors (I, II, III, and IV). Each quadrant of the QD photosensitive surface will produce a matching photocurrent when it is illuminated by the incident light. When the light spot moves on the photosensitive surface of the detector, the light spot deviates from the center of the QD. The output currents of the four quadrants are different [30,31]. The light spot's movement can be used to calculate the misalignment angle [32].

The working principle of the four-quadrant detector is shown in Fig. 4.

The pitch angle and yaw angle of the laser echo are θ_e andθ_a, respectively. The photocurrents areI_a,I_b,I_c, andI_d, respectively. Suppose that the spot center is(x_0, y_0), and d_x and d_y are defined as the position error signals on the x and y axes. d_x and d_y can be calculated as follows [2,33]:

$$d_x = \frac{(I_a + I_d) - (I_b + I_c)}{I_a + I_b + I_c + I_d} \tag{1}$$

$$d_y = \frac{(I_a + I_b) - (I_c + I_d)}{I_a + I_b + I_c + I_d} \tag{2}$$

According to d_x andd_y, the misalignment angle between the target

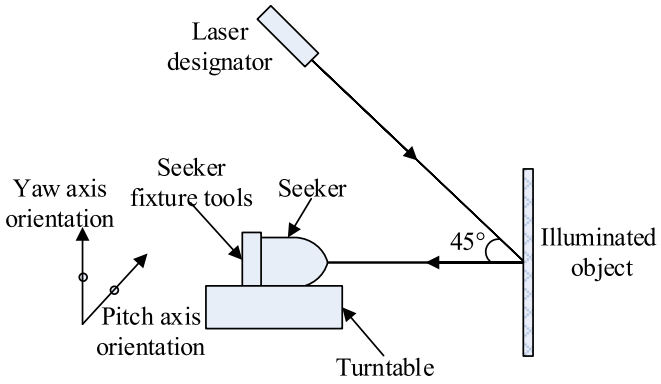

Fig. 6. Schematic diagram of the laser irradiation and reception analysis.

and the optical axis on the x-axis and y-axis can be calculated using the trigonometric relationship. $\theta_e = \arctan(d_x/f)$ and $\theta_a = \arctan(d_y/f)$ are the pitch angle and yaw angle, respectively, where f is the focal length of the seeker optical system. If the optical mechanism is certain, f is a constant. As a result, the pitch angle and yaw angle match up with where the spot center is located on the photosensitive surface.

2.2. Error analysis of the misalignment angle

As illustrated in Fig. 5, the basic components of the semi-active laser seeker are a laser optical subsystem, a gyro-stabilized platform, and a servo control subsystem. The mechanism error [34], measurement error, environmental factors, and other types of errors are the main sources of error for the misalignment angle.

First, the mechanical errors are analyzed. The seeker system is a two-gimbal structure with a sophisticated optical electromechanical integration system. The issue of a non-vertical axis and system misalignment in the system might be brought by machining defects and assembly problems in the system. This error response can be defined as Δd_x andΔd_y.

The system contains sensors such as detectors and gyro, which inevitably produce measuring errors. Thus, the final pitch angle and yaw angle of the system will produce errors $\Delta\theta_a$ and$\Delta\theta_e$, respectively.

Environmental errors are caused by a variety of factors, including workplace vibration, temperature, and overload. In the end, each of the aforementioned issues contributes to the misalignment angle inaccuracy.

3. Calibration strategy

This section describes the calibration model calculation and calibration compensation. This study fully utilizes the output of the turntable and the stabilized platform to offer calibration for the misalignment angle in order to increase calibration accuracy.

3.1. Model for calibration

A schematic diagram of laser irradiation and reception analysis is presented in Fig. 6. The inner frame of the turntable is mounted with the semi-active laser seeker. The initial position is preset through the movement of the turntable. The center axis of the seeker, the center axis of the fixture, and the center ring axis of the turntable all coincide. Second, the turntable is made to rotate step by step at the initially predetermined angle within the seeker's whole range of vision. The yaw angle θ_{ap} and pitch angle θ_{ep} of the turntable are recorded at each step. Meanwhile, the seeker measures the pitch misalignment angle θ_e and the yaw misalignment angleθ_a. The designed detection field of view is $\pm\theta_{\text{lim}}$(this value must be determined according to the actual field of view of the seeker. Here, it is taken as an integer to illustrate the problem.).

In Fig. 7, a schematic representation of the seeker's field of vision traversal mode is displayed. The analysis of Fig. 7(a) and 7(b) is provided below. The lattice that must be traversed is shown in Fig. 7(a), and the interval between two adjacent points is1°. The traversal direction is depicted in Fig. 7(b). The turntable is driven to revolve incrementally at the first predetermined angle$(-\theta_{\text{lim}}, -\theta_{\text{lim}})$. The step size of each step is$\Delta\theta$. Here $\Delta\theta$ is taken as$\Delta\theta = 1^\circ$. The step length can be chosen based on the current circumstance. The turntable moves in the following order. First, the turntable moves from $(-\theta_{\text{lim}}, -\theta_{\text{lim}})$ as the starting point to$(-\theta_{\text{lim}}, +\theta_{\text{lim}})$, and then from $((-\theta_{\text{lim}} + 1^\circ), -\theta_{\text{lim}})$ as the starting point to$((-\theta_{\text{lim}} + 1^\circ), +\theta_{\text{lim}})$. The turntable moves according to this rule until the end point$(+\theta_{\text{lim}}, +\theta_{\text{lim}})$. Every time the turntable spins to a point, the misalignment angle at the current angle and the turntable's actual feedback angle are recorded. To get an averaged result, each point is sampled many times.

The recorded value of the turntable is shown in Eq. (3):

$$\theta_T = \begin{bmatrix} \theta_{T1,1} & \theta_{T1,2} & \cdots & \theta_{T1,(2\theta_{\text{lim}}+1)} \\ \theta_{T2,1} & \ddots & \theta_{T2,2\theta_{\text{lim}}} & \theta_{T2,(2\theta_{\text{lim}}+1)} \\ \vdots & \vdots & \ddots & \vdots \\ \theta_{T(2\theta_{\text{lim}}+1),1} & \cdots & \theta_{T(2\theta_{\text{lim}}+1),2\theta_{\text{lim}}} & \theta_{T(2\theta_{\text{lim}}+1),(2\theta_{\text{lim}}+1)} \end{bmatrix} \tag{3}$$

where the subscript T indicates that the turntable rotates, and $\theta_{Ti,j} =$

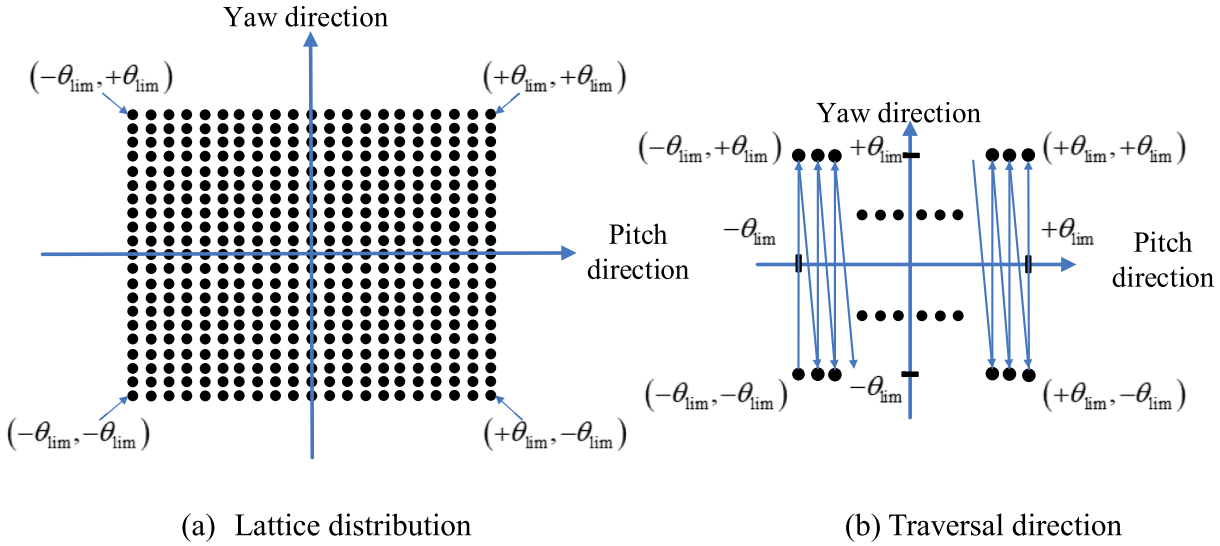

Fig. 7. Schematic diagram of the field of view traversal mode of the seeker.

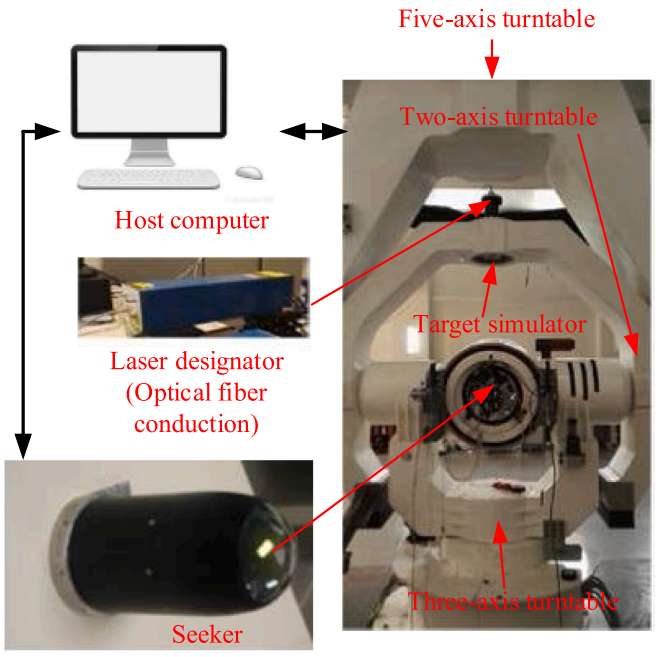

Fig. 8. Calibration experimental system.

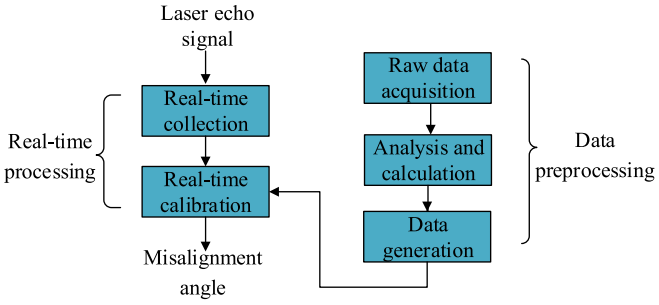

Fig. 9. Calibration flow chart.

$\left[\theta_{Tei,j} \quad \theta_{Tai,j}\right]$ $(i = 1\cdots(2\theta_{\lim}+1); j = 1\cdots(2\theta_{\lim}+1))$ defines the pitch and yaw angle of the turntable at a specific position. The subscript e indicates elevation, and the subscript a indicates azimuth. The recorded value of the stabilized platform is shown in Eq. (4):

$$\theta_S = \begin{bmatrix} \theta_{S1,1} & \theta_{S1,2} & \cdots & \theta_{S1,(2\theta_{\lim}+1)} \\ \theta_{S2,1} & \ddots & \theta_{S2,2\theta_{\lim}} & \theta_{S2,(2\theta_{\lim}+1)} \\ \vdots & \vdots & \ddots & \vdots \\ \theta_{S(2\theta_{\lim}+1),1} & \cdots & \theta_{S(2\theta_{\lim}+1),2\theta_{\lim}} & \theta_{S(2\theta_{\lim}+1),(2\theta_{\lim}+1)} \end{bmatrix} \tag{4}$$

where the subscript S indicates the rotation of the seeker, and $\theta_{Si,j} = \left[\theta_{Sei,j} \quad \theta_{Sai,j}\right]$ $(i = 1\cdots(2\theta_{\lim}+1); j = 1\cdots(2\theta_{\lim}+1))$ defines the pitch and yaw angle matrix of the seeker at a specific position.

Remark: The actual pitch and yaw angles corresponding to each position are measured multiple times and then averaged. The aim is to reduce the influence of random errors caused by vibration, temperature changes, and electrical noise in the experiments on system calibration.

The row index $1 \sim (2\theta_{\lim}+1)$ of θ_T indicates that the turntable's pitch angle is from $-\theta_{\lim}$ to $+\theta_{\lim}$, and the step angle is1°. The column index $1 \sim (2\theta_{\lim}+1)$ of θ_T indicates that the turntable's yaw angle is from $-\theta_{\lim}$ to $+\theta_{\lim}$, and the step angle is1°.

The row index $1 \sim (2\theta_{\lim}+1)$ of θ_S indicates that the seeker's pitch angle is from $-\theta_{\lim}$ to $+\theta_{\lim}$, and the step angle is1°. The column index $1 \sim (2\theta_{\lim}+1)$ of θ_S indicates that the seeker's yaw angle is from $-\theta_{\lim}$ to $+\theta_{\lim}$, and the step angle is1°.

Here, a calibration function $f(\cdot)$ is constructed to calibrate the pitch misalignment angle. The pitch angle and yaw angle of θ_S are taken as input variables, and all the pitch angles of θ_T are taken as output variables of the function. The calibration function is constructed as follows:

$$z_p = f(x_p, y_y) \tag{5}$$

where z_p is the pitch angle$z_p = \theta_{Tei,j}$, x_p is the pitch angle$x_p = \theta_{Sei,j}$, and y_y is the yaw angle$y_y = \theta_{Sai,j}$. The surface is constructed to fit the function$z_p = f\left(x_p, y_y\right)$, and then the entire field of view is uniformly meshed. As a result, the pitch angle array is generated. The data of θ_T and θ_S are obtained through actual experiments, and then $f(\cdot)$ can be calculated through Eq. (5).

Here, a calibration function $h(\cdot)$ is constructed to calibrate the yaw misalignment angle. The pitch angle and yaw angle of θ_S are taken as input variables, and all the yaw angles are taken as output variables of the function. The calibration function is constructed as follows:

$$t_y = h(x_p, y_y) \tag{6}$$

where t_y is the yaw angle of$t = \theta_{Tai,j}$. The surface is constructed to fit the function$t_y = h\left(x_p, y_y\right)$, and then the entire field of view is uniformly meshed. As a result, the yaw angle array is generated. The data of θ_T and θ_S are obtained through actual experiments, and then $h(\cdot)$ can be calculated through Eq. (6).

3.2. Lowess algorithm

To obtain the required $z_p = f\left(x_p, y_y\right)$ and $t_y = h\left(x_p, y_y\right)$ based on the measured data, the algorithm used here is the Lowess algorithm. The Lowess algorithm is a non-parametric regression method. When predicting a new sample, it retrains the samples according to the new weight. The data obtain new parameter values, and the parameter values for each prediction are different.

The objective function of linear or polynomial regression is as follows:

$$J(\theta) = \frac{1}{2}\sum_{i=1}^{m}\left(h_\theta\left(x^{(i)}\right) - y^{(i)}\right)^2 \tag{7}$$

where m is the total sampling point, $e_i = h_\theta\left(x^{(i)}\right) - y^{(i)}$ is the system residual,$y^{(i)}$ is the sampling value $y^{(i)}$ at the i−th sampling point, and $h_\theta\left(x^{(i)}\right)$ is the regression function. As the sample size is continuously increased, the parameters won't alter once they've been established. The optimization problem is to find the appropriate parameters θ to minimize the above loss function.

Locally weighted regression, on the other hand, gives a specific weight to each point close to the predicted point. Similar to linear regression, this subset also adopts ordinary regression which is performed based on the minimum mean square error. The objective function now becomes [35]:

$$J(\theta) = \frac{1}{2}\sum_{i=1}^{m} w^{(i)}\left(h_\theta\left(x^{(i)}\right) - y^{(i)}\right)^2 \tag{8}$$

Here $w^{(i)}$ is the weight, not the regression coefficient. For each prediction, the algorithm must choose the appropriate data subset beforehand. The value of the weight is related to the value of$x$. That is, when calculating the estimated value of each y of$x$, the above equation will change [9,16]. The kernel function is frequently used to give neighboring points more weight. The kernel type can be selected freely. The Gaussian kernel function is the most popular kernel function, and the weights are as follows:

$$w^{(i)} = \exp\left(-\frac{\left(x^{(i)} - x\right)^2}{2\tau^2}\right) \tag{9}$$

where x is the newly predicted sample feature data, and $x^{(i)}$ is the

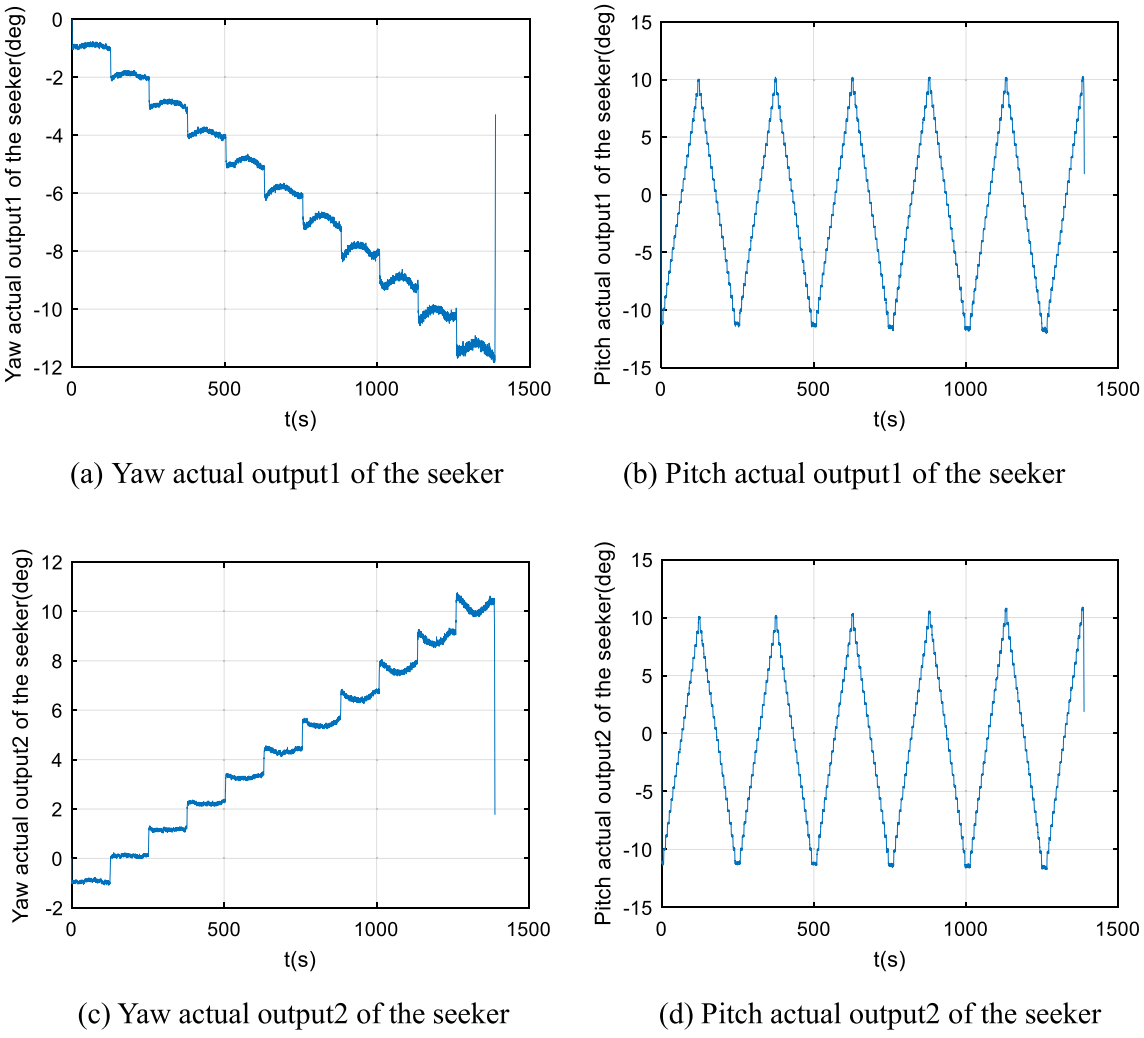

Fig. 10. Raw data obtained from the experiment.

sample point. τ is called the wavelength parameter, and it controls the rate of the weight. If τ is larger, the falling speed will be very slow. If τ is smaller, the falling speed will be very fast.

w is a matrix of m*m consisting of only diagonal elements. The nature of the weight value is that: if the point closer is to the prediction sample data, x has a larger weight, and if the point is farther away from the prediction sample data, x has a smaller weight. Naturally, locally weighted regression will update the parameters when a new sample is predicted in order to improve the accuracy of the prediction. The result of using this weight calculation approach is to prioritize the precise fitting of nearby points while ignoring the contribution of those points farther away [17,35].

3.3. Interpolation method

In this section, the calibration compensation will be implemented by combining the fitted data with the actual measurement data. The data step size after fitting is chosen asΔ. The traversal angle is $-\theta_{\lim} \sim +\theta_{\lim}$. The number of grid points in the pitch direction and yaw direction of the seeker is$n = 2*\frac{\theta_{\lim}}{\Delta} + 1$. As mentioned above, the array $z_{p0}[n][n]$ is constructed by the fitting output of the Lowess algorithm. The process for estimating the calibration value is as follows. To begin with, the index value is calculated using the angle value that the seeker directly measured. The pitch angle that is actually measured is set asP_A, and the yaw angle that is actually measured is set asY_A. Here, *INDEX_R* is set as the row index of the two-dimensional array of the pitch angle and is rounded to:

$$INDEX_R = \langle P_A * \theta_{\lim} + 100 \rangle \tag{10}$$

where the angle bracket "⟨⟩" means rounding the data within it. *INDEX_C* is set as the column index of the two-dimensional array of the yaw angle and is rounded to:

$$INDEX_C = \langle Y_A * \theta_{\lim} + 100 \rangle \tag{11}$$

As a result, the expression $PY_A = z_{p0}[INDEX_R][INDEX_C]$ can be used to determine the calibrated pitch anglePY_A. The calibrated pitch angle can be obtained by looking up the data in$z_{p0}[n][n]$. In the same way, to obtain the yaw calibration angle, it needs to replace $z_{p0}[n][n]$ with$t_{y0}[n][n]$. The calibrated yaw angle YP_A is$YP_A = t_{y0}[INDEX_R][INDEX_C]$. The calibrated pitch angle can be obtained by looking up the data in$t_{y0}[n][n]$.

If the necessary calibration misalignment angle cannot be found in the index value, the linear interpolation method is used. The interpolation model used is shown in Eq. (12):

$$Y = Y_1 + \frac{(Y_2 - Y_1)(X - X_1)}{(X_2 - X_1)} \tag{12}$$

where (X_1, Y_1) and (X_2, Y_2) are two known points in $z_{p0}[n][n]$ or$t_{y0}[n][n]$. If X is known, Y corresponding to X can be obtained by Eq. (12).

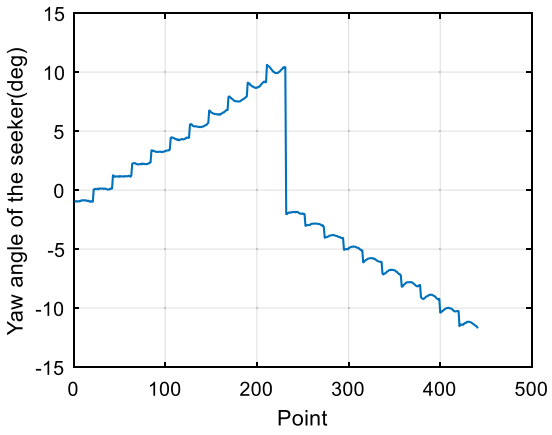

(a) Average output of the yaw angle of the seeker

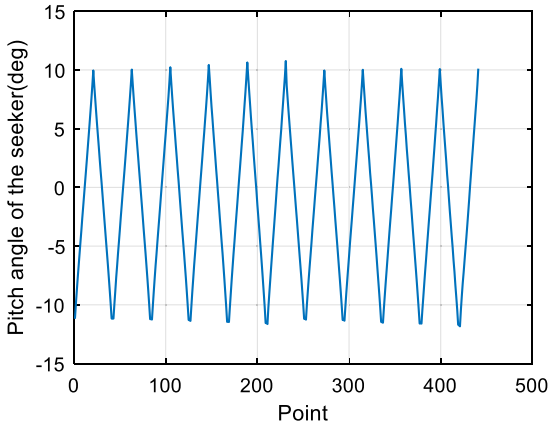

(b) Average output of the pitch angle of the seeker

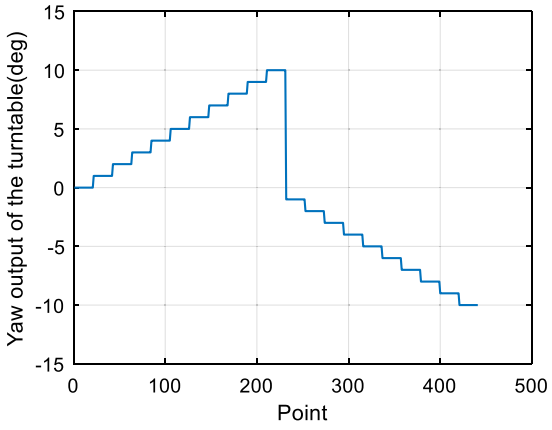

(c) Yaw output of the turntable

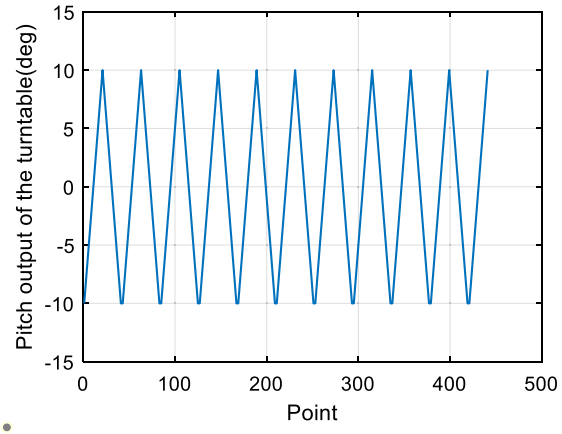

(d) Pitch output of the turntable

Fig. 11. Average value of the system raw data.

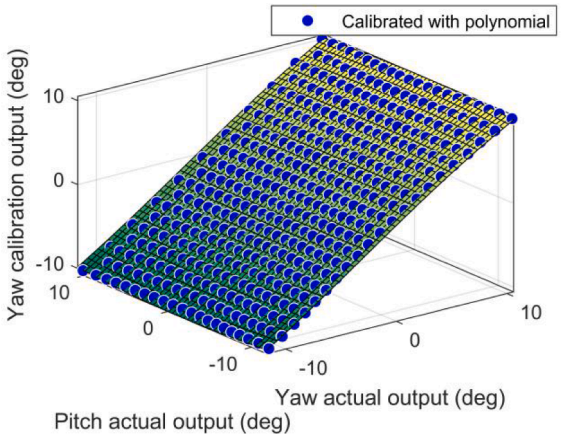

(a) Yaw calibration output by the polynomial algorithm algorithm

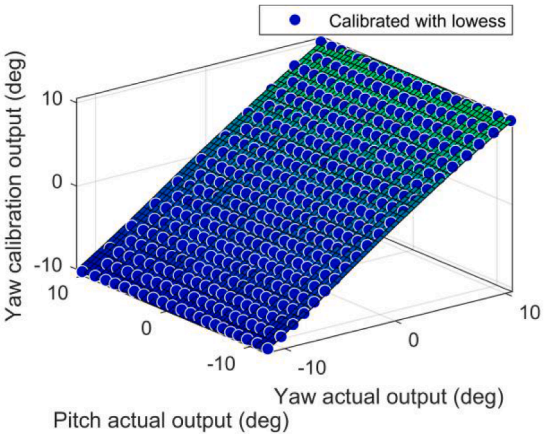

(b) Yaw calibration output by the Lowess

Fig. 12. Yaw calibration output.

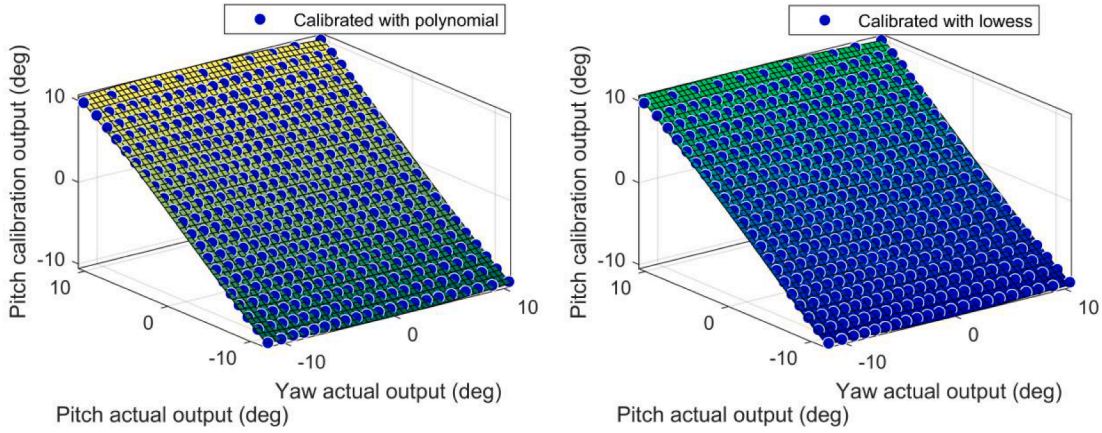

(a) Pitch calibration output by the polynomial algorithm

(b) Pitch calibration output by the Lowess algorithm

Fig. 13. Pitch calibration output.

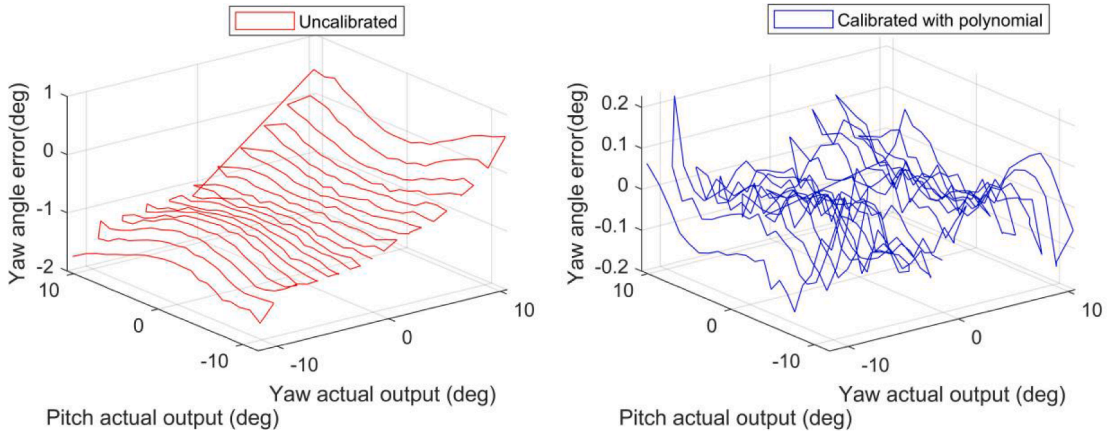

(a) Uncalibrated data

(b) Calibrated with polynomial

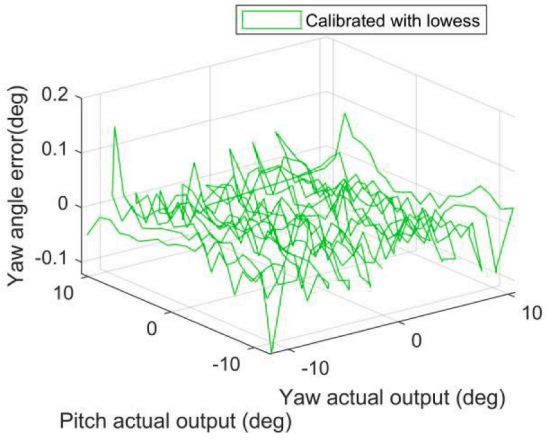

(b) Calibrated with Lowess

Fig. 14. Yaw angle error.

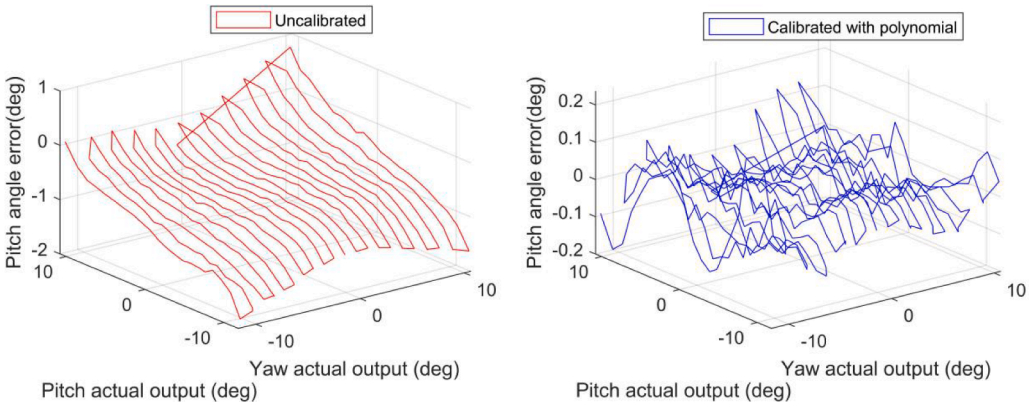

(a) Uncalibrated data

(b) Calibrated with polynomial

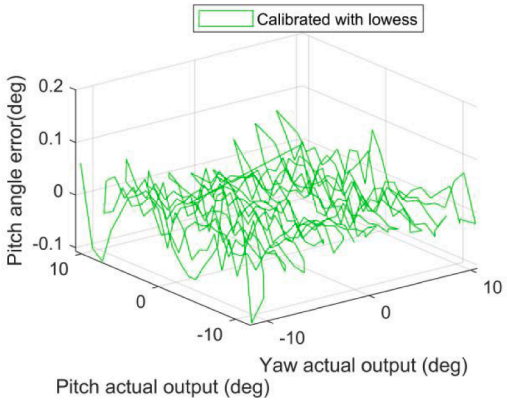

(b) Calibrated with Lowess

Fig. 15. Pitch angle error.

Table 1
Comparison of yaw and pitch axis fitting performance.

Algorithm	Yaw axis	Pitch axis
Polynomial (Goodness of fit)	R-square: 0.9999 Adjusted R-square: 0.9999 RMSE: 0.05585	R-square: 0.9999 Adjusted R-square: 0.9999 RMSE: 0.04664
Lowess (Goodness of fit)	R-square: 1 Adjusted R-square: 1 RMSE: 0.02778	R-square: 1 Adjusted R-square: 1 RMSE: 0.02811

Table 2
Comparison of the yaw angle and pitch angle error.

Axis	Algorithm	Max/deg	Std/deg	Mean value/deg
Yaw	Uncalibrated	0.6189	0.3721	−0.7675
	Calibrated with polynomial	0.2264	0.0558	-9.65×10^{-4}
	Calibrated with Lowess	0.1401	0.0278	1.73×10^{-16}
Pitch	Uncalibrated	0.7632	0.3972	−0.6680
	Calibrated with polynomial	0.2358	0.0466	-4.43×10^{-4}
	Calibrated with Lowess	0.1485	0.0281	3.31×10^{-16}

4. Experimental results and analysis

4.1. Experimental system settings

Fig. 8 depicts the experimental apparatus, wherein the laser guidance uses a semi-active approach.

As depicted in Fig. 8, the experimental apparatus consists of a seeker, a five-axis turntable (containing two and three axes), a host computer, a laser designator, and a target simulator. The system elements in Fig. 8 are consistent with the semi-active laser guidance principle in Fig. 2. The host PC transmits commands and receives the motion state. The seeker is mounted on a three-axis turntable so that the optical axis can move continuously in the pitch direction and the yaw direction. As a target simulator for the two-axis turntable, the end of the laser designator is mounted to the inner frame. This simulates the diffusely reflected laser. The host PC sends the instruction to the three-axis platform. Then, the three-axis platform rotates. The seeker rotates and follows the target simulator. Finally, the motion states of the three-axis turntable and the seeker are recorded.

For data interaction, this system uses FPGA and DSP processors. Target identification, adaptive gate control, anti-jamming, and other tasks are being carried out concurrently by the FPGA. DSP calculates the pitch and yaw misalignment angle and accomplishes the integration simultaneously. The seeker's field of view angle range is chosen first, as seen in Fig. 7. The pitch angle ranges from -10° to $+10^\circ$. The yaw angle ranges from -10° to $+10^\circ$. The roll function of the three-axis turntable is not used. The pitch angle range of the three-axis turntable is from -12° to $+16^\circ$. The yaw angle range of the three-axis turntable is from -30° to $+30^\circ$. To ensure the calibration accuracy of the misalignment angle within 1°, an interval of 1° is set here. The reflection coefficient of the diffuse reflector is 0.2. The laser emitting device emits energy in the range of 4 μJ ∼ 1 mJ.

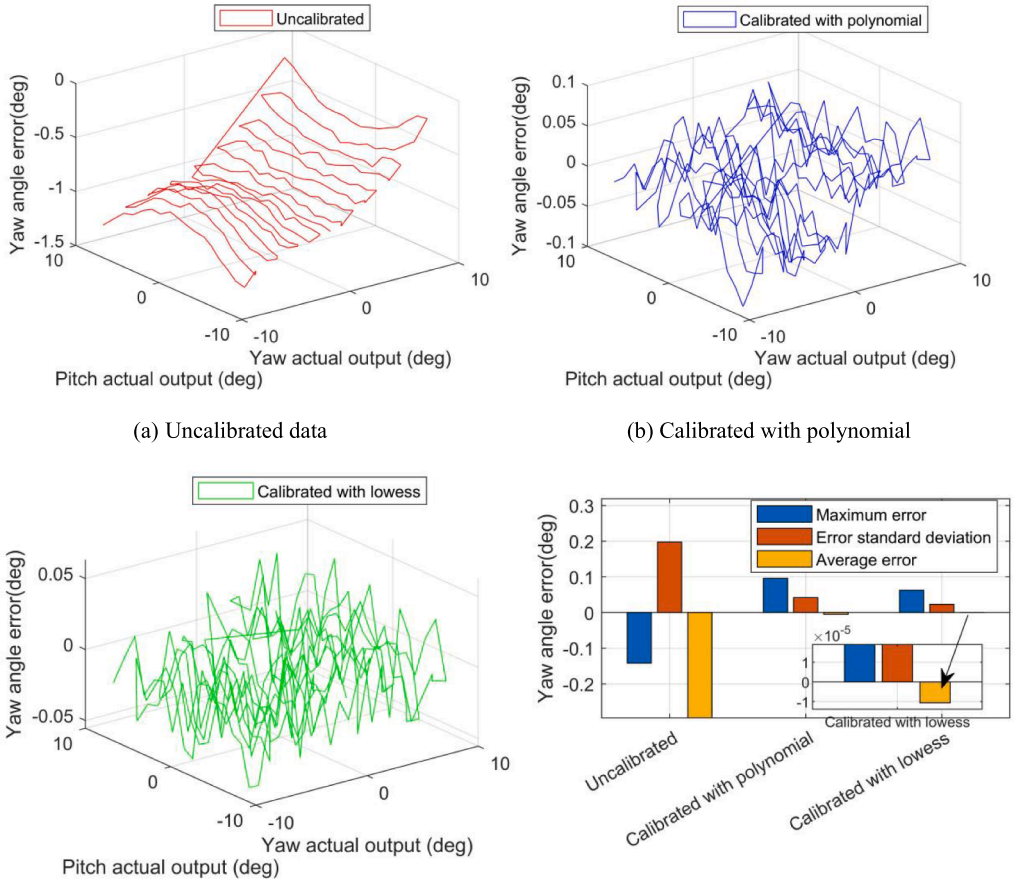

(a) Uncalibrated data (b) Calibrated with polynomial

(c) Calibrated with Lowess (d) Error comparison before and after yaw axis calibration

Fig. 16. Error analysis before and after yaw axis calibration.

4.2. Calibration process and analyses

The calibration process is depicted in Fig. 9. The specific process is divided into the following procedures: data preprocessing and real-time processing.

(1) Data preprocessing

The turntable control program is written to make the optical axis of the seeker point traverse the entire field of view of the seeker. The specific traversal method is illustrated in Fig. 7. In this experiment, the three-axis turntable moves from (−10°, −10°) to (−10°, +10°) and then from (−9°, −10°) to (−9°, +10°). The three-axis turntable moves according to this rule until the end point (+10°, +10°). Every time the turntable rotates to a location, the seeker measures the laser misalignment angle at the current angle and records it together with the turntable's actual feedback angle. One hundred data values are needed for averaging.

This part uses the traversal process shown in Fig. 7. We record data and calculate the calibration function according to Eq. (3–6). Fig. 10 shows the actual value of the full stroke of each measurement. Fig. 10 (a) depicts the actual yaw output of the seeker from 0~11°. Fig. 10 (b) depicts the actual pitch output of the seeker corresponding to the actual yaw output (shown in Fig. 10(a)). Fig. 10(c) depicts the seeker's actual yaw output from −1 ~ -10°. Fig. 10(d) depicts the seeker's actual pitch output, which corresponds to the seeker's actual yaw output (shown in Fig. 10(c)).

The number of the measurements is 100. The samples are obtained and averaged. The pitch angle and yaw angle of the seeker are depicted in Fig. 11 (a-b). The output data of the turntable are depicted in Fig. 11 (c-d).

The data shown in Fig. 11 are used to establish the calibration model. Third-order and two-variable polynomial, and Lowess algorithms are used as the two fitting algorithms to fit the $z_p = f\left(x_p, y_y\right)$ and $t_y = h\left(x_p, y_y\right)$. The fitting curve is depicted in Fig. 12 and Fig. 13, respectively. The calibration strategy used here is explained in Section 3.3. Both the polynomial and Lowess fitting methods make use of this linear interpolation technique. Therefore, the difference between the calibration methods is the fitting method. In Fig. 12 and Fig. 13, uncalibrated, polynomial calibration, and Lowess calibration are used for better expression.

Figs. 14 and 15 show, respectively, the yaw angle error and pitch angle error. Table 1 provides a comparison of the yaw and pitch axis fitting results. Here are the comparisons between R-square, modified R-square, and root mean squared error (RMSE). Table 1 presents the results of the data processing in Fig. 14 and Fig. 15. R-square and adjusted R-square values near 1 suggest greater fitting performance. A lower RMSE value denotes greater fitting performance. The quantitative indicators used to examine the results shown in Fig. 14 and Fig. 15 are R-square, adjusted R-square, and RMSE values. Table 1 demonstrates that in terms of goodness of fitting, the Lowess performs better than polynomials.

In Table 2, the system's comparative performance data are displayed. The maximum value (Max), the standard deviation value (Std), and the average value (Mean) are analyzed and compared in Table 2. The system operates more effectively in terms of fitting when the maximum value, standard deviation, and average value are lower. The

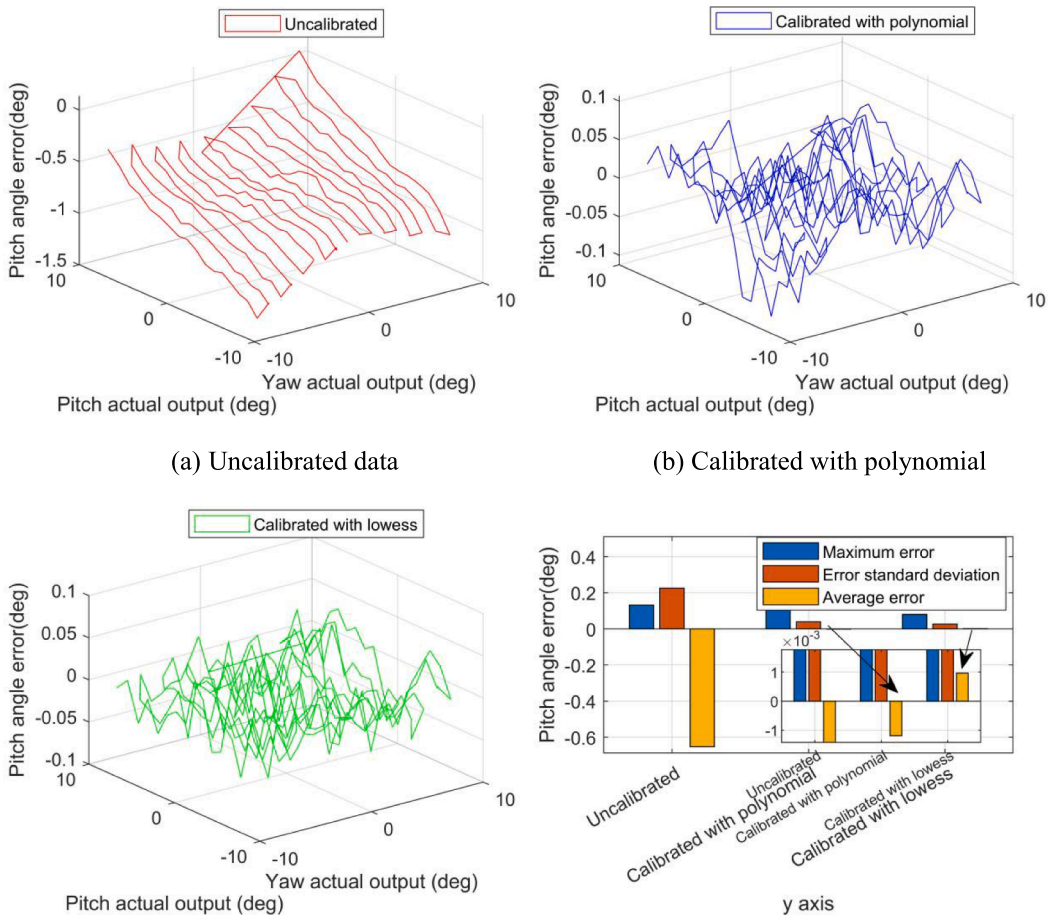

(a) Uncalibrated data (b) Calibrated with polynomial

(c) Calibrated with Lowess (d) Error comparison before and after pitch axis calibration

Fig. 17. Error analysis before and after pitch axis calibration.

quantitative indices used to evaluate the outcomes in Fig. 14 and Fig. 15 are the maximum value, standard deviation value, and average value. According to Table 2, the calibrated error is lower than the uncalibrated system's error. As may be shown, Lowess performs better than polynomials. The following outcomes can be obtained by contrasting the uncalibrated system with the system calibrated using the Lowess method. The maximum value of the yaw angle error changed from 0.6189° to 0.1401°. The standard deviation value changed from 0.3721° to 0.278°. The average value changed from −0.7675 to 1.73×10^{-16}°. The maximum deviation of the pitch angle error changed from 0.7632° to 0.1485°. The standard deviation value changed from 0.3972° to 0.0281°. The average value changed from −0.6680° to 3.31×10^{-16}°. Evidently, Lowess calibration greatly improves misalignment angle accuracy.

4.3. Verification of the proposed method

This section demonstrates a series of experiments traversing from −8° to + 8°. The new sample data are predicted by the established model described in Section 4.3. The calibration error of the yaw angle is shown in Fig. 16(a-c). After the statistics of the above errors are established, a histogram is shown in Fig. 16(d). The calibration error of the pitch angle is shown in Fig. 17(a-c). After the statistics of the above errors are established, a histogram is shown in Fig. 17(d). As can be observed, the Lowess calibration also results in a decreased error for the predicted data. This outcome demonstrates that the system data can be calibrated using the fitted model. These results serve as the foundation for putting the methods described in Section 4.4 into practice.

4.4. Real-time processing

This part is built on the interpolation strategy that is discussed in Section 3.3. The pitch angle array and yaw angle array that were acquired in Section 4.2 are configured on the embedded system. Both of the pitch and yaw angle ranges are −10° to + 10°, and the grid spacing is 0.1°. In the seeker's pitch and yaw directions, there are 201 and 201 grid points, respectively.

The Lowess algorithm's fitting output is used to build the array$z_{p0}[201][201]$. The interpolation process is outlined below. The index value is first computed using the seeker's measurement of the misalignment angle. The actual measured pitch angle is set asP_A, and the actual measured yaw angle is set asY_A. As a result, the row index *INDEX_R* is rounded toP_A*10 + 100. The column index *INDEX_C* is rounded toY_A*10 + 100. Therefore, the calibrated pitch angle PY_A can be obtained by$PY_A = z_{p0}[INDEX_R][INDEX_C]$. The calibrated value can be obtained by looking up the data$PY_A = z_{p0}[INDEX_R][INDEX_C]$.

The array $t_{y0}[201][201]$ is built by fitting the Lowess algorithm's output. The interpolation process is outlined below. The index value is first computed using the seeker's measurement of the misalignment angle. The actual measured pitch angle is set asP_A, and the actual measured yaw angle is set asY_A. As a result, the row index *INDEX_R* is rounded toP_A*10 + 100. The column index *INDEX_C* is rounded toY_A*10 + 100. Therefore, the calibrated yaw angle YP_A can be obtained by$YP_A = t_{y0}[INDEX_R][INDEX_C]$. The calibrated value can be obtained by looking up the data$YP_A = t_{y0}[INDEX_R][INDEX_C]$. The linear interpolation method is used if the misalignment angle that needs to be calibrated cannot be found in the index value.

5. Conclusion

The photoelectric signal is processed to calculate the misalignment angle. The accuracy of the misalignment angle is a critical issue for the laser seeker. The interpolation method and Lowess regression strategy are used here to improve the accuracy of the misalignment angle, in contrast to other previously published works on the subject. Experiments are carried out to verify the effectiveness of the strategy. The theory and the aforementioned experimental results make it abundantly evident that the approach suggested in this research greatly improves the accuracy of the misalignment angle. The main drawback of the research described in this paper is the existence of inaccurate calibrated measurements. (1) Linear interpolation is used in the procedure to calibrate the system. When the fitted model drastically changes, the linear interpolation is inaccurate. (2) The traversal step size is crucial. The calibration error should be minimized by using a smaller step size. (3) The calibration method used in this study makes the assumption that the system's nonlinear components are mostly constant and don't change much during the course of the seeker's entire displacement stroke. In practice, some nonlinear components undergo significant modification. Real-time adaptive calibration will significantly reduce the calibration error. In the future, we will investigate adaptive calibration methods to reduce calibration error by considering structural assembly factors and external disturbance factors of the entire system.

Funding

This work was funded by Shandong Province Natural Science Foundation, China, (Grant No. ZR2021QF031), and Jilin Provincial Science and Technology Department Foundation, China, (Grant No. 20210508038RQ).

CRediT authorship contribution statement

Mingyue Zhang: Conceptualization, Formal analysis, Resources, Writing – original draft, Supervision, Funding acquisition. **Hui Liu:** Methodology, Software, Validation, Writing – review & editing. **Yongliang Guan:** Supervision, Writing – review & editing. **Qingdang Li:** Writing – review & editing. **Zhen Sun:** .

Declaration of Competing Interest

The authors declare that they have no known competing financial interests or personal relationships that could have appeared to influence the work reported in this paper.

Data availability

Data will be made available on request.

References

[1] J. Waldmann, Line-of-sight rate estimation and linearizing control of an imaging seeker in a tactical missile guided by proportional navigation, IEEE Trans. Control Syst. Technol. 10 (2002) 556–567, https://doi.org/10.1109/TCST.2002.1014675.
[2] Y. Zheng, H. Chen, Z. Zhou, Angle measurement of objects outside the linear field of view of a strapdown semi-active laser seeker, Sensors 18 (2018) 1–12, https://doi.org/10.3390/s18061673, 1673.
[3] J.M. Hilkert, Inertially stabilized platform technology concepts and principles, IEEE Control Syst. Mag. 28 (2008) 26–46, https://doi.org/10.1109/MCS.2007.910256.
[4] C. Yang, Y. Yanli, S. Tingting, C. Hairong, M. Xikui, Error analysis of direct writing calibration system for laser seeker, Infrared Laser Eng. 48 (2019) 1105007-1–1105007-8, https://doi.org/10.3788/IRLA201948.1105007.
[5] K. Qi, Z. Huang, J. Wang, L. Ke, Design of a four-quadrant detector for the laser seeker of guided gun-launched projectile, Opt. Sens. Imag. Technol. Appl. 10462 (2017) 1046214-1–1046214-8, https://doi.org/10.1117/12.2283259.
[6] C. Song, C. Ji, S. Li, Y. Wu, Q. Chen, A decoupling three-position calibration method based on observability analysis for SINS/CNS integrated navigation, IEEE Sens. J. 22 (2022) 15284–15295, https://doi.org/10.1109/JSEN.2022.3187246.
[7] D. Yuan, Y. Ding, J. Zhang, Calibration of seeker angle-measuring error with block three-order polynomial, AcArm 40 (2019) 2042–2049, https://doi.org/10.3969/j.issn.1000-1093.2019.10.009.
[8] J. Tong, X. Xu, T. Zhang, Y. Li, Y. Yao, C. Weng, L. Hou, L. Zhang, Xiaosu Tao, Zhang Yao, Yiqing Chengcheng, Weng Lanhua, A misalignment angle error calibration method of underwater acoustic array in strapdown inertial navigation system/ultrashort baseline integrated navigation system based on single transponder mode, Rev. Sci. Instrum. 90 (8) (2019) 085001-1–085001-13, https://doi.org/10.1063/1.5100250, 085001.
[9] X. Dong, L. Gao, X. Shen, Passing azimuth vertically with the technique of magnetooptic modulation, Acta Photon. Sin. 30 (2001) 1389–1391, doi: CNKI:SUN:GZXB.0.2001-11-021.
[10] M. Smolik, V. Skala, O. Nedved, A comparative study of LOWESS and RBF approximations for visualization, in: International Conference on Computational Science and Its, Applications,Springer International Publishing, 2018, pp. 405–419.
[11] C. Qinggui, Research of gridding angle calibration for a strapdown laser seeker, Henan, Sci. Technol. 777 (2021) 15–19, https://doi.org/10.19968/j.cnki.hnkj.1003-5168.2022.07.003.
[12] J. Liu, H. Li, S. Ma, J. Luo, B. Fu, F. Zhang, Simultaneous calibration method for doppler velocity log errors based on a genetic algorithm, IEEE Sens. J. 22 (10) (2022) 9558–9567, https://doi.org/10.1109/JSEN.2022.3155932.
[13] H. Gao, C. Gao, G. Zhao, A robust H ∞ approach of in-flight calibration for UAVs with low-cost IMU, JPC 1187 (2019) 1–7, https://doi.org/10.1088/1742-6596/1187/4/042101, 04101.
[14] S. Aoyagi, M. Suzuki, T. Takahashi, J. Fujioka, Y. Kamiya, Calibration of kinematic parameters of robot arm using laser tracking system: compensation for non-geometric errors by neural networks and selection of optimal measuring points by genetic algorithm, Int. J. Auto Tech-Jpn. 6 (1) (2012) 29–37, https://doi.org/10.20965/ijat.2012.p0029.
[15] L. Huang, W. Ma, J. Huang, Modeling and calibration of pointing errors with alt-az telescope, NewA 47 (2016) 105–110, https://doi.org/10.1016/j.newast.2016.02.007.
[16] B. Berthelot, E. Grivel, P. Legrand, New variants of DFA based on LOESS and LOWESS methods: Generalization of the detrending moving average, in: ICASSP 2021 - 2021 IEEE International Conference on Acoustics, Speech and Signal Processing (ICASSP), (2021) 5140-5144, doi: 10.1109/ICASSP39728.2021.9414216.
[17] E. Pintus, S. Sorbolini, A. Albera, G. Gaspa, C. Dimauro, R. Steri, G. Marras, N.P. P. Macciotta, Use of locally weighted scatterplot smoothing (LOWESS) regression to study selection signatures in Piedmontese and Italian Brown cattle breeds, Anim. Genet. 45 (1) (2014) 1–11, https://doi.org/10.1111/age.12076.
[18] Z. Yi, N. Pan, Y. Liu, Y. Guo, Study of laser displacement measurement data abnormal correction algorithm, EngCo 34 (2017) 123–133, https://doi.org/10.1108/EC-10-2015-0325.
[19] R. Zhang, Q. Meng, S. Lu, A temperature filtering algorithm for cement burning belt based on local weighted regression, 2017 4th International Conference on Information Science and Control Engineering (ICISCE), (2017) 821-824,doi: 10.1109/ICISCE.2017.175.
[20] X. Du, Q. Xia, The calibration method of phased array seeker with the phantom-bit technology, Optik – Int. J. Light Electron Opt. 127 (2016) 7225–7234, https://doi.org/10.1016/j.ijleo.2016.05.066.
[21] B. Zhang, H. Chu, T. Sun, L. Guo, Thermal calibration of a tri-axial MEMS gyroscope based on Parameter-Interpolation method, Sens. Actuators, A 261 (2017) 103–116, https://doi.org/10.1016/j.sna.2017.04.013.
[22] P. Aggarwal, Z. Syed, X. Niu, N. El-Sheimy, A standard testing and calibration procedure for low cost mems inertial sensors and units, JNav 61 (2008) 323–336, https://doi.org/10.1017/S0373463307004560.
[23] J. Kang, B. Wu, Z. Sun, J. Wang, Calibration method of laser beam based on discrete point interpolation for 3D precision measurement, OExpr 28 (2020) 27588–27599, https://doi.org/10.1364/OE.403160.
[24] Ying Bai, Dali Wang, On the comparison of trilinear, cubic spline, and fuzzy interpolation methods in the high-accuracy measurements, Fuzzy Syst. IEEE Trans. 18 (5) (2010) 1016–1022, https://doi.org/10.1109/tfuzz.2010.2064170.
[25] J. Qi, B. Chen, D. Zhang, A calibration method for enhancing robot accuracy through integration of kinematic model and spatial interpolation algorithm, J. Mech. Roboti. 13 (6) (2021) 1–27, https://doi.org/10.1115/1.4051061.
[26] C. Liu, Q. Sun, W. Dai, Z. Ren, Q. Li, F. Yu, Sun Qiucheng, Dai Weiyu, Ren Zeming, Li Qingliang, Yu Fanhua, A method of camera calibration based on kriging interpolation, IEEE Access 9 (2021) 153540–153547, https://doi.org/10.1109/access.2021.3127221.
[27] A. Beatrici, E.D. Beatrici, Hydrostatic buoyancy correction and calibration points interpolation using tare weights, JPC 1826 (1) (2021) 1–7, https://doi.org/10.1088/1742-6596/1826/1/012076, 012076.
[28] Y. Xu, E. Xu, Additive calibration model for NO2 based on linear interpolation, JPC 1616 (1) (2020) 1–7, https://doi.org/10.1088/1742-6596/1616/1/012071, 012071.
[29] Y. Xu, E. Xu, ARIMA based on linear interpolation for SO2 monitoring data's calibration, J. Phys.: Conf. Ser. 1616 (1) (2020) 1–6, https://doi.org/10.1088/1742-6596/1616/1/012044, 012044.
[30] M. Toyoda, Measurement of the characteristics of a quadrant avalanche photodiode and its application to a laser tracking system, OptEn 41 (2002) 145–149, https://doi.org/10.1117/1.1418222.
[31] Y. Panduputra, T.W. Ng, A. Neild, M. Robinson, Intensity influence on Gaussian beam laser based measurements using quadrant photodiodes, ApOpt 49 (2010) 3669–3675, https://doi.org/10.1364/AO.49.003669.

[32] W. Nelson, J.P. Palastro, C. Wu, C.C. Davis, Using an incoherent target return to adaptively focus through atmospheric turbulence, OptL 41 (2016) 1301–1304, https://doi.org/10.1364/OL.41.001301.
[33] X. Cheng, Y. Yang, Q. Hao, Analysis of the effects of thermal environment on optical systems for navigation guidance and control in supersonic aircraft based on empirical equations, Sensors 16 (10) (2016) 1–16, https://doi.org/10.3390/s16101717, 1717.
[34] W.S. Cleveland, Robust locally weighted regression and smoothing scatterplots, Publ. Am. Stat. Assoc. 74 (1979) 829–836, https://doi.org/10.1080/01621459.1979.10481038.